



**HAL**  
open science

## Order from disorder phenomena in BaCoS<sub>2</sub>

Benjamin Lenz, Michele Fabrizio, Michele Casula

► **To cite this version:**

Benjamin Lenz, Michele Fabrizio, Michele Casula. Order from disorder phenomena in BaCoS<sub>2</sub>. Communications Physics, 2024, 7 (1), pp.35. 10.1038/s42005-023-01514-4 . hal-04397716

**HAL Id: hal-04397716**

**<https://hal.science/hal-04397716v1>**

Submitted on 16 Jan 2024

**HAL** is a multi-disciplinary open access archive for the deposit and dissemination of scientific research documents, whether they are published or not. The documents may come from teaching and research institutions in France or abroad, or from public or private research centers.

L'archive ouverte pluridisciplinaire **HAL**, est destinée au dépôt et à la diffusion de documents scientifiques de niveau recherche, publiés ou non, émanant des établissements d'enseignement et de recherche français ou étrangers, des laboratoires publics ou privés.

# Order from disorder phenomena in BaCoS<sub>2</sub>

Benjamin Lenz<sup>1\*</sup>, Michele Fabrizio<sup>2</sup> and Michele Casula<sup>1</sup>

<sup>1</sup>IMPMC, Sorbonne Université, CNRS, MNHN, 4 place Jussieu, Paris, F-75005, France.

<sup>2</sup>International School for Advanced Studies (SISSA), Via Bonomea 265, Trieste, I-34136, Italy.

\*Corresponding author(s). E-mail(s):

[benjamin.lenz@sorbonne-universite.fr](mailto:benjamin.lenz@sorbonne-universite.fr);

Contributing authors: [fabrizio@sissa.it](mailto:fabrizio@sissa.it);

[michele.casula@sorbonne-universite.fr](mailto:michele.casula@sorbonne-universite.fr);

## Abstract

At  $T_N \simeq 300$  K the layered insulator BaCoS<sub>2</sub> transitions to a columnar antiferromagnet that signals non-negligible magnetic frustration despite the relatively high  $T_N$ , all the more surprising given its quasi two-dimensional structure. Here, we show, by combining *ab initio* and model calculations, that the magnetic transition is an order-from-disorder phenomenon, which not only drives the columnar magnetic order, but also the inter-layer coherence responsible for the finite Néel transition temperature. This uncommon ordering mechanism, actively contributed by orbital degrees of freedom, hints at an abundance of low energy excitations above and across the Néel transition, in agreement with experimental evidence.

## 1 Introduction

Frustrated magnets often display a continuous accidental degeneracy of the classical ground state that leads to the appearance of pseudo-Goldstone modes within the harmonic spin-wave approximation [1]. Since those modes are not protected by symmetry, they may acquire a mass once anharmonic terms are included in the spin-wave Hamiltonian. This mass, in turn, cuts off the singularities brought about by the pseudo-Goldstone modes, in that way stabilising ordered phases otherwise thwarted by fluctuations. To put it differently, let us imagine that the classical potential has

30 a manifold of degenerate minima generally not invariant under the symmetry group  
 31 of the Hamiltonian. It follows that the eigenvalues of the Hessian of the potential  
 32 change from minimum to minimum. Allowing for quantum or thermal fluctuations is  
 33 therefore expected to favour the minima with lowest Hessian determinant, although  
 34 the two kinds of fluctuations not necessarily select the same ones [2]. Moreover, it  
 35 is reasonable to assume that the minima with lowest Hessian determinant are those  
 36 that form subsets invariant under a symmetry transformation of the Hamiltonian so  
 37 that choosing any of them corresponds to a spontaneous symmetry breaking. Such a  
 38 phenomenon, also known as order from disorder [3], emerges in many different con-  
 39 texts [4], from particle physics [5, 6] to condensed matter physics [7, 8], even though  
 40 frustrated magnets still provide the largest variety of physical realisations [1–3, 9–15].

41  
 42 The layered insulator  $\text{BaCoS}_2$  might be legitimately included in the class of frus-  
 43 trated magnets. Below a critical temperature  $T_N$ ,  $\text{BaCoS}_2$  becomes an antiferromagnet  
 44 characterised by columnar spin-ordered planes, which we hereafter refer to as antifer-  
 45 romagnetic striped (AFS) order, a classic symptom of frustration. The planes are in  
 46 turn stacked ferromagnetically along the  $c$ -axis, so called C-type stacking as opposed  
 47 to the antiferromagnetic G-type one. Inelastic neutron scattering (INS) experiments  
 48 show that magnetic excitations below  $T_N$  have pronounced two-dimensional (2D)  
 49 character [16, 17] implying strong quantum and thermal fluctuations that join with  
 50 magnetic frustration to further hamper magnetic order. In spite of all that, the Néel  
 51 temperature of  $\text{BaCoS}_2$  is rather large, between 290 K [18] and 305 K [19], which is  
 52 highly surprising. Indeed, a direct estimate of the spin exchange constants by neutron  
 53 diffraction has been recently attempted in doped tetragonal  $\text{BaCo}_{0.9}\text{Ni}_{0.1}\text{S}_{1.9}$  subject  
 54 to an uniaxial strain [17]. This compound undergoes a Néel transition to the C-type  
 55 AFS phase at 280 K [17], not far from  $T_N$  of undoped  $\text{BaCoS}_2$ . The neutron data  
 56 were fitted by a conventional  $J_1 - J_2$  Heisenberg model [13] on each plane plus an  
 57 inter-plane ferromagnetic exchange  $J_c$ , yielding  $J_2 \sim 9.3$  meV,  $J_1 \sim -2.3$  meV and  
 58  $0 < |J_c| < 0.04$  meV, with the upper bound due to experimental resolution. The Néel  
 59 temperature can be overestimated discarding  $J_1$  [20] and taking  $|J_c|$  equal to the upper  
 60 bound. In that way, one obtains [21]  $T_N \simeq 200$  K, which, despite supposedly being an  
 61 overestimate, is 2/3 smaller than the observed value. This discrepancy is puzzling.

62 Another startling property is the anomalously broad peak of the magnetic suscepti-  
 63 bility at  $T_N$  [18, 19], which suggests a transition in the Ising universality class rather  
 64 than the expected Heisenberg one [19]. A possible reason of this behaviour might be  
 65 spin-orbit coupling [19]. Indeed, a Rashba effect due to the layered structure and  
 66 the staggered sulfur pyramid orientation, see Fig. 1, has been found to yield sizeable  
 67 band splittings at specific points within the Brillouin zone, at least in metallic tetrag-  
 68 onal  $\text{BaNiS}_2$  [22]. The Rashba-like spin-orbit coupling strength may barely differ in  
 69  $\text{BaCoS}_2$ , or be weakened by strong correlations [23]. In either case, its main effect is  
 70 to introduce an easy plane anisotropy, as indeed observed experimentally [19], which,  
 71 at most, drives the transition towards the  $XY$  universality class. It is well possible  
 72 that the weak orthorhombic distortion in  $\text{BaCoS}_2$  may turn the easy plane into an  
 73 easy axis, but the resulting magnetic anisotropy should be negligibly small and thus  
 74 unable to convincingly explain the experimental observations.

75 Lastly, BaCoS<sub>2</sub> shows a very strange semiconducting behaviour above  $T_N$ , with acti-  
76 vated dc conductivity, no evidence of a Drude peak and, yet, an optical conductivity  
77 that grows linearly in frequency [24].

78  
79 The relatively high  $T_N$  despite magnetic frustration and quasi-two dimensional  
80 character, as well as the abundance of low energy excitations above and across the  
81 Néel transition are pieces of evidence that some kind of order-from-disorder phe-  
82 nomenon takes place in BaCoS<sub>2</sub>, a scenario that we here support by a thorough  
83 analysis combining *ab initio* and model calculations.

## 85 2 Results

### 86 2.1 Phase diagram of BaCoS<sub>2</sub>

87 BaCoS<sub>2</sub> is a metastable layered compound that, quenched from high temperature,  
88 crystallises in an orthorhombic structure with space group  $Cmme$ , no. 67 [25], charac-  
89 terised by in-plane primitive lattice vectors  $a \neq b$ . However, we believe physically more  
90 significant to consider as reference structure the higher-symmetry non-symmorphic  
91  $P4/nmm$  tetragonal one ( $a = b$ ) of the opposite end member, BaNiS<sub>2</sub>, and regard  
92 the orthorhombic distortion as an instability driven by the substitution of Ni with  
93 the more correlated Co. The hypothetical tetragonal phase of BaCoS<sub>2</sub> is shown in  
94 Fig. 1(A). Each CoS  $a - b$  plane has two inequivalent cobalt atoms, Co(1) and Co(2),  
95 see Fig. 1(B), which are related to each other by a non-symmorphic symmetry.

96 Below  $T_N$ , an AFS magnetically ordered phase sets in. In the  $a - b$  plane it consists of  
97 ferromagnetic chains, either along  $a$  (AFS-a) or  $b$  (AFS-b), coupled antiferromagnet-  
98 ically, see Fig. 1(C). The stacking between the planes is C-type, i.e., ferromagnetic,  
99 thus the labels C-AFS-a and C-AFS-b that we shall use, as well as G-AFS-a and  
100 G-AFS-b whenever we discuss the G-type configurations with antiferromagnetic stack-  
101 ing. We mention that the orthorhombic distortion with  $b > a$  ( $a > b$ ) is associated  
102 with C-AFS-a (C-AFS-b), i.e., ferromagnetic bonds along  $a$  ( $b$ ) [19], at odds with the  
103 expectation that ferromagnetic bonds are longer than antiferromagnetic ones. This  
104 counterintuitive behaviour represents a key test for the *ab initio* calculations that we  
105 later present.

106 Neutron scattering refinement and magnetic structure modelling in the low-  
107 temperature phase point to an ordered moment of  $\mu_{Co} \sim 2.63 - 2.9\mu_B$  [19, 26],  
108 suggesting that each Co<sup>2+</sup> is in a  $S = 3/2$  spin configuration, in agreement with  
109 the high-temperature magnetic susceptibility [19]. Moreover, the form factor analysis  
110 of the neutron diffraction data [26] indicates that the three 1/2-spins lie one in the  
111  $d_{3z^2-r^2}$ , the other in the  $d_{x^2-y^2}$ , and the third either in the  $d_{xz}$  or  $d_{yz}$  3d-orbitals of  
112 Co. Since  $d_{xz}$  and  $d_{yz}$ , which we hereafter denote shortly as  $x$  and  $y$  orbitals, form in  
113 the  $P4/nmm$  tetragonal structure a degenerate  $E_g$  doublet occupied by a single hole,  
114 such degeneracy is going to be lifted at low-temperature. That hints at the existence of  
115 some kind of orbital order, besides the spin one, in the magnetic orthorhombic phase.  
116 Let us try to anticipate by symmetry arguments which kind of order can be stabilised.  
117 We observe that in the  $Cmme$  orthorhombic structure the cobalt atoms occupy

118 the Wyckoff positions  $4g$ , which, for convenience, we denote as  $\text{Co}(1) \equiv (0, 0, z)$ ,  
 119  $\text{Co}(2) \equiv (1/2, 0, -z)$ ,  $\text{Co}(3) \equiv (0, 1/2, -z)$ ,  $\text{Co}(4) \equiv (1/2, 1/2, z)$ , and have symme-  
 120 try  $mm2$ . As a consequence, the hole must occupy either the  $x$  orbital or the  $y$  one,  
 121 but not a linear combination, and the chosen orbital must be the same for  $\text{Co}(1)$  and  
 122  $\text{Co}(4)$ , as well as for  $\text{Co}(2)$  and  $\text{Co}(3)$ . Therefore, we denote as  $d_n$ ,  $d = x, y$ , the orbital  
 123 occupied by the hole on  $\text{Co}(n)$ ,  $n = 1, \dots, 4$ , and as  $d_1d_2d_3d_4$  a generic orbital con-  
 124 figuration. Then, there are only four of them that are symmetry-allowed:  $xxxx$ ,  $yyyy$ ,  
 125  $xyyx$  and  $yxyx$ , see Fig. 2.

126 We remark that  $xxxx$  is degenerate with  $yyyy$  in the tetragonal phase. The choice of  
 127 either of them is associated with the same  $C_4 \rightarrow C_2$  symmetry breaking that charac-  
 128 terises both the AFS-a or AFS-b spin order and the orthorhombic distortion,  $b > a$  or  
 129  $a > b$ . All these three choices can be associated with three Ising variables  $\tau$ ,  $\sigma$  and  $X$   
 130 such that  $\tau = +1$  corresponds to  $xxxx$ ,  $\sigma = +1$  to AFS-a,  $X = +1$  to  $b > a$ , and vice  
 131 versa. Since they all have the same symmetry, odd under  $C_4$ , they would be coupled  
 132 to each other should we describe the transition by a Landau-Ginzburg functional. We  
 133 shall hereafter denote as  $Z_2(C_4)$  the Ising sector that describes the  $C_4 \rightarrow C_2$  symme-  
 134 try breaking.

135 The other two allowed orbital configurations  $xyyx$  and  $yxyx$  (see Fig. 2) are instead  
 136 degenerate both in the tetragonal and orthorhombic phases, but break the non-  
 137 symmorphic symmetry (NS) that connects, e.g.,  $\text{Co}(1)$  with  $\text{Co}(2)$  and  $\text{Co}(3)$ . We can  
 138 therefore associate to those configurations a new Ising sector  $Z_2(\text{NS})$ .

139 We emphasise that the above conclusions rely on the assumption of a  $Cmme$   
 140 space group. A mixing between  $x$  and  $y$  orbitals is instead allowed by the  $Pba2$  space  
 141 group proposed in Ref. [27] as an alternative scenario for  $\text{BaCoS}_2$  at room temper-  
 142 ature. As a matter of fact, the two symmetry-lowering routes,  $P4/nmm \rightarrow Cmme$   
 143 and  $P4/nmm \rightarrow Pba2$ , correspond to different Jahn-Teller-like distortions involving  
 144 the  $d_{xz}$ - $d_{yz}$  doublet and the  $E_g$  phonon mode of the  $P4/nmm$  structure at the  $\mathbf{M}$   
 145 point, which is found to have imaginary frequency by *ab initio* calculations [27]. How-  
 146 ever, latest high-accuracy X-ray diffraction data [18] confirm the  $Cmme$  orthorhombic  
 147 structure even at room temperature, thus supporting our assumption.

## 148 2.2 *Ab initio* analysis

149 Using density functional theory (DFT) and DFT+U calculations, in the first place,  
 150 we checked if the tetragonal phase is unstable towards magnetism, considering both a  
 151 conventional Néel order (AFM) compatible with the bipartite lattice and the observed  
 152 AFS. We found, using a Hubbard interaction of  $U = 2.8$  eV and a Hund's coupling  
 153 constant  $J = 0.95$  eV for the Co-3d orbitals as motivated by constrained random  
 154 phase approximation (cRPA) [24], that the lowest energy state is indeed the AFS, the  
 155 AFM and non-magnetic phases lying above by about 0.5 eV and 2.3 eV, respectively.  
 156 Let us therefore restrict our analysis to AFS and stick to  $U = 2.8$  eV. Note, however,  
 157 that the ordering of the four configurations with lowest energy within our DFT+U  
 158 simulations does not change within 2 eV around that value. The main assumptions  
 159 entering our *ab initio* modelling are thereby not sensitive to the precise choice of  $U$   
 160 around the value motivated by cRPA calculations. We use an 8-site unit cell that  
 161 includes two planes, which allows us to compare C-AFS with G-AFS. In addition, we

162 consider both the tetragonal structure with AFS-a, since AFS-b is degenerate, and  
 163 the orthorhombic structure with  $b > a$ , in which case we analyse both AFS-a and  
 164 AFS-b. For all cases, we investigate all four symmetry-allowed orbital configurations,  
 165  $xxxx$ ,  $yyyy$ ,  $xyyx$  and  $yxyx$ , assuming either a C-type or G-type orbital stacking  
 166 between the two planes of the unit cell, so that, for instance,  $G(xxxx)$  means that  
 167 one plane is in the  $xxxx$  configuration and the other in the  $yyyy$  one.

168  
 169 In Table 1 we report the energies per formula unit of several possible configurations  
 170 in the tetragonal structure, including those that would be forbidden in the orthorhom-  
 171 bic one. All energies are measured with respect to the lowest energy state and are  
 172 expressed in Kelvin. In agreement with experiments, the lowest energy state T0 has  
 173 spin order C-AFS, a or b being degenerate. In addition, it has C-type antiferro-orbital  
 174 order,  $C(xyxx)$ . We note that its G-type spin counterpart T1 is only 2 K above, sup-  
 175 porting our observation that  $T_N = 290$  K is anomalously large if compared to these  
 176 magnetic excitations. The abundance of nearly degenerate ground states is consistent  
 177 with the seminal DFT+U study by Zainullina and Korotin [28], where the importance  
 178 of different orbital configurations for a given stripe magnetic phase was studied for a  
 179 larger value of  $U$ .

180 The energy differences between C-type orbital stacked configurations and their G-type  
 181 counterparts are too small to allow obtaining a reliable modelling of the inter-plane  
 182 orbital coupling. On the contrary, the energy differences between in-plane orbital con-  
 183 figurations can be accurately reproduced by a rather simple modelling. We assume on  
 184 each Co-site an Ising variable  $\tau_3$  equal to the difference between the hole occupations  
 185 of orbital  $x$  and of orbital  $y$ . The Ising variable on a given site is coupled only to  
 186 those of the four nearest neighbour sites in the  $a - b$  plane, with exchange constants  
 187  $\Gamma_{1a} = \Gamma_1 + \sigma \delta\Gamma_1$  and  $\Gamma_{1b} = \Gamma_1 - \sigma \delta\Gamma_1$  along  $a$  and  $b$ , respectively. In addition, the  
 188 Ising variables feel a uniform field  $B_\tau \sigma$ . Here,  $\sigma$  is the Ising  $Z_2(C_4)$  order parameter  
 189 that distinguishes AFS-a,  $\sigma = +1$  from AFS-b,  $\sigma = -1$ . We find that the spectrum is  
 190 well reproduced by the parameters in Table 2. It is worth noticing that the in-plane  
 191 antiferro-orbital order is unexpected in light of the nematic columnar spin order that  
 192 would rather suggest the ferro-orbital  $xxxx$  or  $yyyy$  configurations to have lowest  
 193 energy. The explanation is that the antiferro-orbital order yields within DFT+U a  
 194 larger insulating gap than the ferro-orbital order, see Fig.3.

195  
 196 We now move to the physical orthorhombic structure, assuming  $b > a$  with  
 197  $b/a = 1.008$  [25], and recalculate all above energies but considering only the orbital  
 198 configurations allowed by the  $Cmme$  space group. In this case, we have to distinguish  
 199 between AFS-a and AFS-b, which are no longer degenerate. The results are shown in  
 200 Table 3.

201 The calculated magnetic moment per Co atom in the lowest energy state, O0 in  
 202 Table 3, is  $\mu_{AFS} \sim 2.65 \mu_B$ , in quite good agreement with experiments [19, 26]. We  
 203 remark that the *ab initio* calculation correctly predicts that the lowest energy state O0  
 204 has ferromagnetic bonds along  $a$  despite  $b > a$ , which, as we mentioned, is an impor-  
 205 tant test for the theory. The energy difference between AFS-a and AFS-b, i.e., O0 and  
 206 O3, is about 20 K, and gives a measure of the spin-exchange spatial anisotropy in the

207  $a$  and  $b$  directions due to the orthorhombic distortion. This small value implies that  
 208 the Néel transition temperature  $T_N \simeq 290$  K is largely insensitive to the orthorhombic  
 209 distortion that exists also above  $T_N$  [18, 19]. In particular, the energy difference  
 210 between C-type and G-type stacking, O0 and O1 in Table 3, remains the same tiny  
 211 value found in the tetragonal phase. Table 3 thus suggests that the spin configurations  
 212 C-AFS-a, C-AFS-b, G-AFS-a and G-AFS-b are almost equally probable at the Néel  
 213 transition, and that despite the orthorhombic structure.

214 The orbital arrangement of the C-AFS-a configuration is also important to describe,  
 215 e.g., the pressure-induced metal-insulator transition in BaCoS<sub>2</sub>, see Supplementary  
 216 Note 1.

### 217 2.2.1 Orthorhombic distortion.

218 A further evidence of the marginal role played by the orthorhombic distortion at  
 219 the Néel transition comes from the total energy as function of the parameter  $d =$   
 220  $2(a-b)/(a+b)$  that quantifies the distortion, shown in Fig. 4 for different orbital con-  
 221 figurations assuming AFS-a magnetic order. We note that for all orbital configurations  
 222 the energy gain due to a finite  $d$  is tiny with respect to  $d = 0$ . For instance, the lowest-  
 223 energy orbital configuration  $xyyx$  reaches a minimum at about  $d_{\min}^{xyyx} \sim -0.5\%$ , not  
 224 far from the experimental value  $d_{\text{exp}} \sim -0.8\%$  [25], which reduces to  $d_{\text{exp}} \sim -0.4\%$   
 225 under high pressure synthesis [18]. However, the energy gain with respect to  $d = 0$  is  
 226 less than 3 K. This result suggests that, despite the hypothetical  $P4/nmm$  structure  
 227 of BaCoS<sub>2</sub> being inherently unstable to an orthorhombic Jahn-Teller distortion, the  
 228 latter plays almost no role in stabilising the AFS magnetic order in contrast to naïve  
 229 expectations.

### 230 2.2.2 Wannierisation

231 To gain further insight into the mechanisms that drive the Néel transition, we generate  
 232 two tight-binding Hamiltonians with maximally-localised Wannier functions for Co-  
 233  $d$ -like and Co- $d_{xz}/d_{yz}$ -like orbitals, respectively. Both tight-binding models reproduce  
 234 overall well the DFT band structure of the PM phase in the orthorhombic structure,  
 235 see Fig. 5. Whereas the fit of the 5-orbital model is nearly perfect, the 2-orbital model  
 236 shows small deviations along the  $\mathbf{M} - \Gamma$  direction due to missing hybridisation with  
 237 the other Co- $d$  orbitals. Table 4 shows the leading hopping processes of the 5-band  
 238 model restricted to the  $(d_{xz}, d_{yz})$  subspace.

239 We note that, because of the staggered shift of the Co atoms out of the sulfur basal  
 240 plane, the largest intra-layer hopping is between next-nearest neighbour (NNN) cobalt  
 241 atoms instead of nearest-neighbour (NN) ones. Moreover, the stacking of the sulfur  
 242 pyramids and the position of the intercalated Ba atoms makes the inter-layer NN  
 243 hopping negligible, contrary to the NNN one that is actually larger than the in-plane  
 244 NN hopping, but still smaller than the in-plane NNN one ( $t_{NN}^{\text{inter}} \ll t_{NN}^{\text{intra}} < t_{NNN}^{\text{inter}} <$   
 245  $t_{NNN}^{\text{intra}}$ ).

246 We finally remark that the orthorhombic distortion has a very weak effect on the inter-  
 247 layer hopping, which is consistent with the tiny energy difference between C-AFS and  
 248 G-AFS being insensitive to the distortion, compare, e.g., the energies of T1 and O1  
 249 in Tables 1 and 3, respectively.

### 2.3 Effective Heisenberg model

Armed with all the above *ab initio* results, we are now ready to address the main questions of this work, i.e., why  $T_N$  is so high and why the Néel transition looks Ising-like.

We already mentioned that the largest energy scales that emerge from the *ab initio* calculations are the magnetic ones separating the lowest-energy AFS configuration from the Néel and non-magnetic states. Therefore, even though BaCoS<sub>2</sub> seems not to lie deep inside a Mott insulating regime, we think it is worth discussing qualitatively the spin dynamics in terms of an effective  $S = 3/2$  Heisenberg model. If we assume that the leading contribution to the exchange constants derives from the hopping processes within the  $d_{xz} - d_{yz}$  subspace, then Table 4 suggests the Heisenberg model shown in Fig. 6. According to this figure, the exchange constants  $J_{1x/y}$ ,  $J_2$ , and  $J_{3x/y}$  are related to the hopping terms  $T_{(\pm 1, 0, 0)/(0, \pm 1, 0)}$ ,  $T_{\pm(1, -1, 0)/\pm(1, 1, 0)}$ , and  $T_{(\pm 1, 0, 1)/(0, \pm 1, 1)}$ , reported in Table 4. This model consists of frustrated  $J_1 - J_2$  planes [13, 29–32] coupled to each other by a still frustrating  $J_3$  coupling, see Fig. 6(b). In order to be consistent with the observed columnar magnetic order, the exchange constants have to satisfy the inequality  $2J_2 > |J_3| + |J_1|$ . Moreover,  $J_3$  forces to deal with a two sites unit cell, highlighted in yellow colour in Fig. 6(a) where the non-equivalent cobalt sites are referred to as Co(1), in blue, and Co(2), in red, respectively. The reason is that Co(1) on a plane is only coupled to Co(2) on the plane above but not below, and vice versa for Co(2).

To simplify the notation, we write, for  $a = 1, 3$ ,  $J_{ax} = J_a (1 - \delta_a)$  and  $J_{ay} = J_a (1 + \delta_a)$ , where, in analogy with the single-layer  $J_1 - J_2$  model [13],  $\delta_a \neq 0$  are Ising order parameters associated with the  $C_4 \rightarrow C_2$  symmetry breaking. Moreover, we define the in-plane Fourier transforms of the spin operators

$$\mathbf{S}_{\ell, n}(\mathbf{q}) = \sum_{\mathbf{R}} e^{-i\mathbf{q} \cdot \mathbf{R}} \mathbf{S}_{\ell, n, \mathbf{R}}, \quad (1)$$

where  $\mathbf{R}$  labels the  $N$  unit cells in the  $a - b$  plane,  $\ell = 1, 2$  the two sites (sublattices) within each unit cell, and  $n = 1, \dots, L$  the layer index. With those definitions, the Hamiltonian reads

$$\begin{aligned} H = \frac{1}{N} \sum_{n\mathbf{q}} \left\{ J_2(\mathbf{q}) \left( \mathbf{S}_{1, n}(\mathbf{q}) \cdot \mathbf{S}_{1, n}(-\mathbf{q}) + \mathbf{S}_{2, n}(\mathbf{q}) \cdot \mathbf{S}_{2, n}(-\mathbf{q}) \right) \right. \\ \left. + J_1 \left( \gamma(\mathbf{q}, \delta_1) \mathbf{S}_{1, n}(\mathbf{q}) \cdot \mathbf{S}_{2, n}(-\mathbf{q}) + H.c. \right) \right. \\ \left. + J_3 \left( \gamma(\mathbf{q}, \delta_3) \mathbf{S}_{1, n}(\mathbf{q}) \cdot \mathbf{S}_{2, n+1}(-\mathbf{q}) + H.c. \right) \right\} \\ \equiv H_2 + H_1 + H_3, \end{aligned} \quad (2)$$

where  $H_a$  is proportional to  $J_a$ ,  $a = 1, 2, 3$ , and

$$\begin{aligned} J_2(\mathbf{q}) &= 2J_2 \cos q_x \cos q_y, \\ \gamma(\mathbf{q}, \delta) &= e^{iq_x} \left[ (1 - \delta) \cos q_x + (1 + \delta) \cos q_y \right]. \end{aligned} \quad (3)$$

The classical ground state corresponds to the three-dimensional modulation wave vector  $(\pi, 0, Q_z) \equiv (0, \pi, Q_z)$ , which describes an antiferromagnetic order within each sublattice on each layer, and where the inter-plane  $Q_z$  is the value that minimises the



282 classical energy per site,  $E(Q_z) = -2J_2 - 2\sqrt{J_1^2\delta_1^2 + J_3^2\delta_3^2 + 2J_1J_3\delta_1\delta_3\cos Q_z}$ . The  
 283 expression of  $E(Q_z)$  shows that inter-layer magnetic coherence sets in only when the  
 284 two Ising-like order parameters,  $\delta_1$  and  $\delta_3$ , lock together. Specifically,  $J_1J_3\delta_1\delta_3 > 0$   
 285 stabilises C-AFS,  $Q_z = 0$ , otherwise G-AFS,  $Q_z = \pi$ . We already know that the  
 286 former is lower in energy, though by only few Kelvins, see Table 3. Moreover, an  
 287 orthorhombic distortion  $b > a$  favours AFS-a, which implies  $J_1\delta_1 + J_3\delta_3 > 0$ , even  
 288 though AFS-b is higher by only 20 K according to DFT+U, see O3 in Table 3.

289  
 290 Using our  $J_1 - J_2 - J_3$  model to fit the INS data of [17] at 200 K, we estimate  $J_2 \simeq 9.3$   
 291 meV,  $J_1 + J_3 \simeq -2.34$  meV,  $J_1\delta_1 + J_3\delta_3 \simeq 0.53$  meV, and  $0 < \sqrt{J_1J_3\delta_1\delta_3} < 0.14$  meV,  
 292 where, we recall, the upper bound is due to experimental resolution. Such small bound  
 293 suggests that the two order parameters  $\delta_1$  and  $\delta_3$  are already formed at 200 K, whereas  
 294 their mutual locking is still suffering from fluctuations. We finally observe that the  
 295 ferromagnetic sign of  $J_1$  and  $J_3$  is consistent with the diagonal hopping matrices in the  
 296 corresponding directions (see Table 4) and the antiferro-orbital order. Estimations of  
 297 the exchange constants based on the DFT+U energies can be found in Supplementary  
 298 Note 2.

### 300 2.3.1 Spin-wave analysis of the $C_4$ symmetric model

301 To better understand the interplay between the  $Z_2$  ( $C_4$ ) Ising degrees of freedom and  
 302 the magnetic order at  $T_N$ , we investigate in more detail the Hamiltonian (2) with  
 303  $\delta_1 = \delta_3 = 0$ , thus  $J_{1x} = J_{1y} = J_1$  and  $J_{3x} = J_{3y} = J_3$ . Since  $J_2 > 0$  is the dominant  
 304 exchange process, the classical ground state corresponds to the spin configuration

$$\mathbf{S}_{i,n}(\mathbf{q}) = NS \mathbf{n}_{3,i,n} \delta_{\mathbf{q},\mathbf{Q}}, \quad i = 1, 2, \quad n = 1, \dots, L, \quad (4)$$

305 where  $S = 3/2$  is the spin magnitude,  $\mathbf{n}_{3,i,n}$  is a unit vector, and  $\mathbf{Q} = (\pi, 0) \equiv (0, \pi)$ ,  
 306 the equivalence holding since  $\mathbf{G} = (\pi, \pi)$  is a primitive in-plane lattice vector for the  
 307 two-site unit cell. In other words, each sublattice on each plane is Néel ordered, and  
 308 its staggered magnetisation  $\mathbf{n}_{3,i,n}$  is arbitrary. We therefore expect that quantum and  
 309 thermal fluctuations may yield a standard order-from-disorder phenomenon [3].

310 Within spin-wave approximation, the spin operators can be written as

$$\begin{aligned} \mathbf{S}_{i,n}(\mathbf{q}) \cdot \mathbf{n}_{3,i,n} &\simeq NS \delta_{\mathbf{q},\mathbf{Q}} - \Pi_{i,n}(\mathbf{q} - \mathbf{Q}), \\ \mathbf{S}_{i,n}(\mathbf{q}) \cdot \mathbf{n}_{1,i,n} &\simeq \sqrt{NS} x_{i,n}(\mathbf{q}), \\ \mathbf{S}_{i,n}(\mathbf{q}) \cdot \mathbf{n}_{2,i,n} &\simeq \sqrt{NS} p_{i,n}(\mathbf{q} - \mathbf{Q}), \end{aligned} \quad (5)$$

311 where  $\mathbf{n}_{1,i,n}$ ,  $\mathbf{n}_{2,i,n}$  and  $\mathbf{n}_{3,i,n}$  are orthogonal unit vectors,  $x_{i,n}^\dagger(\mathbf{q}) = x_{i,n}(-\mathbf{q})$  and  
 312  $p_{i,n}^\dagger(\mathbf{q}) = p_{i,n}(-\mathbf{q})$  are conjugate variables, i.e.,

$$\left[ x_{i,n}(\mathbf{q}), p_{j,m}^\dagger(\mathbf{q}') \right] = i \delta_{i,j} \delta_{n,m} \delta_{\mathbf{q},\mathbf{q}'}, \quad (6)$$

313 and

$$\begin{aligned} \Pi_{i,n}(\mathbf{q} - \mathbf{Q}) &= \frac{1}{2} \sum_{\mathbf{k}} \left( x_{i,n}^\dagger(\mathbf{k}) x_{i,n}(\mathbf{k} + \mathbf{q} - \mathbf{Q}) \right. \\ &\quad \left. + p_{i,n}^\dagger(\mathbf{k}) p_{i,n}(\mathbf{k} + \mathbf{q} - \mathbf{Q}) - \delta_{\mathbf{q},\mathbf{Q}} \right). \end{aligned} \quad (7)$$

314 The three terms of the Hamiltonian (2) thus read, at leading order in quantum  
 315 fluctuations, i.e., in the harmonic approximation,

$$\begin{aligned}
 H_2 &\simeq E_0 + S \sum_{i, \mathbf{n}, \mathbf{q}} \left( J_2(\mathbf{q}) - J_2(\mathbf{Q}) \right) \left( x_{i,n}^\dagger(\mathbf{q}) x_{i,n}(\mathbf{q}) \right. \\
 &\quad \left. + p_{i,n}^\dagger(\mathbf{q} - \mathbf{Q}) p_{i,n}(\mathbf{q} - \mathbf{Q}) \right), \\
 H_1 &\simeq S J_1 \sum_{n, \mathbf{q}} \left( \gamma(\mathbf{q}) \mathbf{X}_{1,n}(\mathbf{q}) \cdot \mathbf{X}_{2,n}(-\mathbf{q}) + H.c. \right), \\
 H_3 &\simeq S J_3 \sum_{n, \mathbf{q}} \left( \gamma(\mathbf{q}) \mathbf{X}_{1,n}(\mathbf{q}) \cdot \mathbf{X}_{2,n+1}(-\mathbf{q}) + H.c. \right),
 \end{aligned} \tag{8}$$

316 where  $E_0 = 2NL S(S+1) J_2(\mathbf{Q})$ ,  $\gamma(\mathbf{q}) = \gamma(\mathbf{q}, \delta = 0)$ , and

$$\mathbf{X}_{i,n}(\mathbf{q}) = \mathbf{n}_{1,i,n} x_{i,n}(\mathbf{q}) + \mathbf{n}_{2,i,n} p_{i,n}(\mathbf{q} - \mathbf{Q}). \tag{9}$$

317 We note that  $H_2$  does not depend on the choice of  $\mathbf{n}_{3,i,n}$ , reflecting the classical acci-  
 318 dental degeneracy, unlike  $H_1 + H_3$ . We start treating  $H_1$  and  $H_3$  within perturbation  
 319 theory. The unperturbed Hamiltonian  $H_2$  can be diagonalised and yields the spin-wave  
 320 dispersion

$$\omega_2(\mathbf{q}) = 2S \sqrt{J_2(\mathbf{0})^2 - J_2(\mathbf{q})^2}. \tag{10}$$

321

322

### 323 2.3.2 Free energy in perturbation theory and quadrupolar coupling

324 The free energy in perturbation theory can be written as  $F = \sum_\ell F_\ell$ , where  $F_\ell$  is of  
 325  $\ell$ -th order in  $H_1 + H_3$ , and  $F_0$  is the unperturbed free energy of the Hamiltonian  $H_2$ .  
 326 Notice that only even-order terms are non vanishing, thus  $\ell = 0, 2, 4, \dots$ . Given the  
 327 evolution operator in imaginary time,

$$S(\beta) = T_\tau \left( e^{-\int_0^\beta d\tau (H_1(\tau) + H_3(\tau))} \right) = \sum_\ell S_\ell(\beta), \tag{11}$$

328 where  $H_a(\tau)$ ,  $a = 1, 3$ , evolves with the Hamiltonian  $H_2$ , the second order correction  
 329 to the free energy is readily found to be

$$\begin{aligned}
 F_2 &= -T \langle S_2(\beta) \rangle \\
 &= -\frac{\Xi_2(T)}{J_2} \sum_n \left[ J_1^2 (\mathbf{n}_{3,1,n} \cdot \mathbf{n}_{3,2,n})^2 + J_3^2 (\mathbf{n}_{3,1,n} \cdot \mathbf{n}_{3,2,n+1})^2 \right],
 \end{aligned} \tag{12}$$

330 where

$$\Xi_2(T) = J_2 S^2 \sum_{\mathbf{q}} T \sum_{\lambda} |\gamma(\mathbf{q})|^2 \frac{J_2(\mathbf{0}) - J_2(\mathbf{q})}{J_2(\mathbf{0}) + J_2(\mathbf{q})} \left( \frac{\omega_2(\mathbf{q})}{\omega_\lambda^2 + \omega_2(\mathbf{q})^2} \right)^2 > 0, \tag{13}$$

331 with  $\omega_\lambda = 2\pi\lambda T$ ,  $\lambda \in \mathbb{Z}$ , bosonic Matsubara frequencies. Even without explicitly  
 332 evaluating  $\Xi_2$ , we can conclude that the free-energy gain at second order in  $H_1 +$   
 333  $H_3$  is maximised by  $\mathbf{n}_{3,1,n} \cdot \mathbf{n}_{3,2,m} = \pm 1$ , with  $m = n, n+1$ , which reduces the  
 334 classical degeneracy to  $4^L$  configurations, where  $L$  is the total number of layers in

335 the system. Such residual degeneracy is split by a fourth order correction to the free  
 336 energy proportional to  $J_1^2 J_3^2$  that reads

$$F_4 = -\frac{J_1^2 J_3^2}{J_2^3} \Xi_4(T) \sum_n (\mathbf{n}_{3,1,n} \cdot \mathbf{n}_{3,2,n}) \quad (14)$$

$$\left[ (\mathbf{n}_{3,1,n} \cdot \mathbf{n}_{3,2,n+1}) + (\mathbf{n}_{3,1,n-1} \cdot \mathbf{n}_{3,2,n}) \right],$$

337 where

$$\Xi_4(T) = 2S^4 J_2^3 T \sum_\lambda \sum_{\mathbf{q}} |\gamma(\mathbf{q}) \gamma(\mathbf{q} + \mathbf{Q})|^2 \frac{\omega_\lambda^2}{(\omega_\lambda^2 + \omega_2(\mathbf{q})^2)^3} > 0. \quad (15)$$

338 We remark that, despite  $\omega_2(\mathbf{q})$  vanishes linearly at  $\mathbf{q} = \mathbf{0}, \mathbf{Q}$ , both  $\Xi_2(T)$  and  $\Xi_4(T)$   
 339 are non-singular.

340 The fourth order correction  $F_4$  in Eq. (14) has a twofold effect: it forces  $\mathbf{n}_{3,1,n} \cdot \mathbf{n}_{3,2,n}$   
 341 to be the same on all layers and, in addition, stabilises a ferromagnetic inter-layer  
 342 stacking. Therefore, the ground state manifold at fourth order in  $H_1 + H_3$  is spanned  
 343 by  $\mathbf{n}_{3,1,n} = \mathbf{n}_3$  and  $\mathbf{n}_{3,2,n} = \sigma \mathbf{n}_3$ , where  $\mathbf{n}_3$  is an arbitrary unit vector reflecting the  
 344 spin  $SU(2)$  symmetry, and  $\sigma = \pm 1$  is associated with the global  $C_4 \rightarrow C_2$  symmetry  
 345 breaking.

346 Similarly to the single-plane  $J_1 - J_2$  model [13], the above results imply that an  
 347 additional term must be added to the semiclassical spin action. Specifically, if we  
 348 introduce the Ising-like fields  $\sigma_n(\mathbf{R}) = \mathbf{n}_{3,1,n}(\mathbf{R}) \cdot \mathbf{n}_{3,2,n}(\mathbf{R})$  and  $\sigma_{n+1/2}(\mathbf{R}) =$   
 349  $\mathbf{n}_{3,1,n}(\mathbf{R}) \cdot \mathbf{n}_{3,2,n+1}(\mathbf{R})$ , Eqs (12) and (14) imply that, at the leading orders in  $J_1$   
 350 and  $J_3$ , the effective action in the continuum limit includes the quadrupolar coupling  
 351 term [13]  
 352

$$A_Q \simeq - \sum_n \int d\mathbf{R} \left\{ \frac{\Xi_2(T)}{T J_2} \left( J_1^2 \sigma_n(\mathbf{R})^2 + J_3^2 \sigma_{n+1/2}(\mathbf{R})^2 \right) \right. \quad (16)$$

$$\left. + \frac{\Xi_4(T) J_1^2 J_3^2}{T J_2^3} \sigma_n(\mathbf{R}) \left( \sigma_{n+1/2}(\mathbf{R}) + \sigma_{n-1/2}(\mathbf{R}) \right) \right\}.$$

353 We expect a 3D Ising transition to occur at a critical temperature  $T_c$ , below which  
 354  $\langle \sigma_n(\mathbf{R}) \rangle = m_1$ ,  $\langle \sigma_{n+1/2}(\mathbf{R}) \rangle = m_3$ , with  $m_1 m_3 > 0$ . In turn, the Ising order should  
 355 bring along the 3D AFS one below a finite Néel temperature bounded from above  
 356 by  $T_c$  [20]. To get a rough estimate of the latter, based on Eq. (16) we assume that,  
 357 upon integrating out the spin degrees of freedom, the classical action describes an  
 358 anisotropic three-dimensional ferromagnetic Ising model with exchange constants  $I_1$   
 359 on layers  $n$ ,  $I_3$  on layers  $n + 1/2$ , and  $I_\perp < I_1, I_3$  between layers. Hereafter, we take  
 360 for simplicity  $J_1 = J_3$ , thus  $I_1 = I_3 \equiv I_\parallel$ .

361 We then note that, for the  $J_1 - J_2 - J_3$  model with  $J_2 \simeq 9.3$  meV and  
 362  $J_1 = J_3 \simeq -1.17$  meV, the 2D Ising critical temperature with  $S = 3/2$  of each layer  $n$   
 363 and  $n + 1/2$  is about  $0.4(S + 1/2)^2 J_2 \simeq 173$  K [30]. This critical temperature corre-  
 364 sponds to  $I_\parallel \simeq 6.6$  meV in the 2D Ising model. The 3D Ising critical temperature  $T_c$   
 365 grows with  $I_\perp$ , reaching 280 K and 345 K at  $I_\perp = 0.5 I_\parallel$  and  $I_\perp = I_\parallel$ , respectively [33],  
 366 which are reassuringly of the same order of magnitude as  $T_N$ .

367

368 However, BaCoS<sub>2</sub> remains orthorhombic above  $T_N$ , which implies that the structural  
 369  $C_4 \rightarrow C_2$  symmetry breaking occurs earlier than magnetic ordering upon cooling.  
 370 Therefore, even though the effects of the orthorhombic distortion on the electronic  
 371 structure are rather small, see Table 4, it is worth repeating the above discussion  
 372 assuming from the start that  $\sigma_n(\mathbf{R}) = \mathbf{n}_{3,1,n}(\mathbf{R}) \cdot \mathbf{n}_{3,2,n}(\mathbf{R}) = 1$  (AFS-a), so that  
 373  $\sigma_{n+1/2}(\mathbf{R}) = \mathbf{n}_{3,1,n}(\mathbf{R}) \cdot \mathbf{n}_{3,2,n+1}(\mathbf{R}) = \mathbf{n}_{3,1,n}(\mathbf{R}) \cdot \mathbf{n}_{3,1,n+1}(\mathbf{R})$ . It follows that the  
 374 quadrupolar term (16) becomes

$$A_Q \simeq - \sum_n \int d\mathbf{R} \left\{ K(T) \left( \mathbf{n}_{3,1,n}(\mathbf{R}) \cdot \mathbf{n}_{3,1,n+1}(\mathbf{R}) \right)^2 \right. \\ \left. + h(T) \mathbf{n}_{3,1,n}(\mathbf{R}) \cdot \mathbf{n}_{3,1,n+1}(\mathbf{R}) \right\}, \quad (17)$$

375 with  $K(T) \gg h(T) > 0$ . The term proportional to  $K(T)$  is bi-quadratic in the origi-  
 376 nal spin operators and, alone, it would drive an Ising-like transition either towards  
 377 C-AFS,  $\mathbf{n}_{3,1,n} \cdot \mathbf{n}_{3,1,n+1} = 1$  or G-AFS,  $\mathbf{n}_{3,1,n} \cdot \mathbf{n}_{3,1,n+1} = -1$ . On the contrary, the  
 378 term proportional to  $h(T)$  is quadratic and yields an inter-layer ferromagnetic coupling  
 379 that stabilises C-AFS, though by only two kelvins according to our DFT+U calcula-  
 380 tions. Therefore, (17) corresponds to an unusual model of coupled Heisenberg layers  
 381 in which the dominant inter-layer coupling is bi-quadratic. We believe that this term  
 382 is responsible of the higher  $T_N$  than the estimate obtained assuming just the small  
 383 ferromagnetic exchange, as earlier discussed, as well as of the pronounced Ising-like  
 384 character of the Néel transition. We also remark that which among C-AFS and G-AFS  
 385 is lower in energy does depend on the orbital configurations, see Table 3. Therefore,  
 386 we expect that the neglected coupling between spins and orbital fluctuations should  
 387 further reduce the already small energy difference between C-AFS and G-AFS.

### 388 3 Conclusion

389 BaCoS<sub>2</sub> is a frustrated magnet with a pronounced two-dimensional character of the  
 390 magnetic excitations that, nonetheless, orders magnetically at a Néel temperature of  
 391  $T_N \sim 300$  K [18, 19] through a second order phase transition more similar to an  
 392 Ising than a Heisenberg one. We have shown that these puzzling features can be  
 393 pieced together within an order-from-disorder scenario that we have uncovered by a  
 394 thorough *ab initio* analysis demonstrating the critical role of the specific Co *d*-orbitals  
 395 involved in magnetism. Although specific to BaCoS<sub>2</sub>, our results might be relevant  
 396 to other spin-frustrated transition metal compounds that also crystallise in the non-  
 397 symmorphic  $P4/nmm$  space group, like, e.g., the iron pnictides. In many (mainly  
 398 electron-doped) iron-based superconductors the disordered phase at high temperature  
 399 first spontaneously breaks  $C_4$  symmetry when cooling below a critical temperature  
 400  $T_{\text{nem}}$ , thus entering a nematic phase [34]. Only at a lower temperature  $T_N < T_{\text{nem}}$ , also  
 401 spin  $SU(2)$  is broken and a stripe-ordered magnetic long-range order emerges [34, 35].  
 402 The Néel temperature can be quite large as in BaCoS<sub>2</sub> or even vanishing within  
 403 experimental accuracy as in FeSe, where  $T_N \neq 0$  is observed only under pressure [36].  
 404 Also from a model point of view, our description of BaCoS<sub>2</sub> fits into the modelling of

405 these materials. Indeed, the key role played by several order parameters in BaCoS<sub>2</sub>  
406 has parallels to the phenomenological Landau free energy description of FeSC [34].  
407 Besides itinerant multi-orbital Hubbard models [37–39], also spin-1 Heisenberg models  
408 conceptually similar to ours have been proposed for iron-based superconductors and  
409 FeSe [40, 41]. There, however, instead of achieving the  $C_4$  symmetry breaking via an  
410 order-from-disorder phenomenon, it is often assumed from the start [42] or by explicitly  
411 adding bi-quadratic spin exchanges [40] that mimic the quadrupolar terms (16).  
412 Moreover, our *ab initio* simulations for BaCoS<sub>2</sub> predict that the lowest-energy phase  
413 has not ferro-orbital order, as often discussed in the context of FeSC, but rather  
414 an anti-ferro orbital ordering that breaks the non-symmorphic symmetry instead of  
415  $C_4$ . Therefore, BaCoS<sub>2</sub> seems to realise a situation where collinear magnetism and  
416 orthorhombicity do not imply orbital nematicity, unless for specific crystal structures  
417 under pressure.

## 418 4 Methods

### 419 Ab initio calculations

420 We carried out *ab initio* DFT and DFT+U calculations using the Quantum  
421 ESPRESSO package [43, 44]. The density functional is of generalized gradient approx-  
422 imation type, namely the Perdew-Burke-Ernzerhof functional [45], on which local  
423 Hubbard interactions and Hund’s coupling terms were added to the Co atoms in case  
424 of the DFT+U within a fully rotational invariant framework [46, 47]. If not stated  
425 otherwise, the geometry of the unit cell and the internal coordinates of the atomic  
426 positions in the orthorhombic structure were those determined experimentally, taken  
427 from Ref. [25]. For non-magnetic calculations, the relative atomic positions were kept  
428 fixed and the in-plane lattice constants  $a = b$  chosen such that the unit cell volume  
429 matched the one of the orthorhombic structure. Co and S atoms are described by  
430 norm-conserving pseudopotentials (PP) with non-linear core corrections, Ba atoms  
431 are described by ultrasoft pseudopotentials. The Co PP contains 13 valence electrons  
432 ( $3s^2, 3p^6, 3d^7$ ), the Ba PP 10 electrons ( $5s^2, 5p^6, 6s^2$ ), and S PPs are in a ( $3s^2, 3p^3$ )  
433 configuration. The plane-waves cutoff has been set to 120Ry and we used a Gaussian  
434 smearing of 0.01Ry. The  $k$ -point sampling of the electron-momentum grid was at  
435 least  $8 \times 8 \times 8$  points in the 8 Co atom supercell.

### 437 Wannier interpolation

438 To determine the band structure and derive an effective low-energy model, we per-  
439 formed a Wannier interpolation with maximally localised Wannier functions [48, 49]  
440 using the Wannier90 package [50]. We constructed Wannier fits based on the non-  
441 magnetic DFT+U calculation using a  $4 \times 4 \times 4$  k-grid with a doubled in-plane unit  
442 cell comprising 4 Co atoms.

443 **Acknowledgments.** We are thankful to H. Abushammala, A. Gauzzi, and Y. Klein  
444 for fruitful discussions. We acknowledge the allocation for computer resources by the  
445 French Grand Équipement National de Calcul Intensif (GENCI) under the project

446 numbers A0110906493 and A0110912043. M.F. acknowledges financial support from  
447 the European Research Council (ERC), under the European Union’s Horizon 2020  
448 research and innovation programme, Grant agreement No. 692670 ”FIRSTORM”.

## 449 **Declarations**

### 450 **Data availability**

451 The data used for generating the figures of the main text and the Supplementary  
452 Information are available from the corresponding author on reasonable request.

### 453 **Competing interests**

454 The authors declare no competing interests.

### 455 **Code availability**

456 The codes used and described in the Methods section are publicly available. The  
457 scripts used for generating the figures are available from the corresponding author on  
458 reasonable request.

### 459 **Contributions**

460 M.C. and B.L. designed the research, B.L. performed the DFT+U calculations and  
461 M.F. developed the model. All authors analysed the data, discussed the results and  
462 wrote the manuscript.

### 463 **Corresponding author**

464 Correspondence to Benjamin Lenz.

## 465 **References**

- 466 [1] Rau, J.G., McClarty, P.A., Moessner, R.: Pseudo-Goldstone Gaps and Order-by-  
467 Quantum Disorder in Frustrated Magnets. *Phys. Rev. Lett.* **121**, 237201 (2018)  
468 <https://doi.org/10.1103/PhysRevLett.121.237201>
- 469 [2] Schick, R., Ziman, T., Zhitomirsky, M.E.: Quantum versus thermal fluctuations  
470 in the fcc antiferromagnet: Alternative routes to order by disorder. *Phys. Rev. B*  
471 **102**, 220405 (2020) <https://doi.org/10.1103/PhysRevB.102.220405>
- 472 [3] Villain, J., Bidaux, R., Carton, J.P., Conte, R.: Order as an effect of disorder. *J. Phys. France* **41**(11), 1263–1272 (1980) <https://doi.org/10.1051/jphys:0198000410110126300>
- 473  
474
- 475 [4] Burgess, C.: Goldstone and pseudo-Goldstone bosons in nuclear, particle and  
476 condensed-matter physics. *Physics Reports* **330**(4), 193–261 (2000) [https://doi.org/10.1016/s0370-1573\(99\)00111-8](https://doi.org/10.1016/s0370-1573(99)00111-8)  
477

- 478 [5] Weinberg, S.: Approximate Symmetries and Pseudo-Goldstone Bosons. Phys.  
479 Rev. Lett. **29**, 1698–1701 (1972) <https://doi.org/10.1103/PhysRevLett.29.1698>
- 480 [6] Coleman, S., Weinberg, E.: Radiative Corrections as the Origin of Spontaneous  
481 Symmetry Breaking. Phys. Rev. D **7**, 1888–1910 (1973) [https://doi.org/10.1103/](https://doi.org/10.1103/PhysRevD.7.1888)  
482 [PhysRevD.7.1888](https://doi.org/10.1103/PhysRevD.7.1888)
- 483 [7] Demler, E., Hanke, W., Zhang, S.-C.:  $SO(5)$  theory of antiferromagnetism and  
484 superconductivity. Rev. Mod. Phys. **76**, 909–974 (2004) [https://doi.org/10.1103/](https://doi.org/10.1103/RevModPhys.76.909)  
485 [RevModPhys.76.909](https://doi.org/10.1103/RevModPhys.76.909)
- 486 [8] Fernandes, R.M., Chubukov, A.V.: Low-energy microscopic models for iron-based  
487 superconductors: a review. Reports on Progress in Physics **80**(1), 014503 (2016)  
488 <https://doi.org/10.1088/1361-6633/80/1/014503>
- 489 [9] Tessman, J.R.: Magnetic Anisotropy at 0°K. Phys. Rev. **96**, 1192–1195 (1954)  
490 <https://doi.org/10.1103/PhysRev.96.1192>
- 491 [10] Belorizky, E., Casalegno, R., Niez, J.J.: Calculation of the Spin Wave Energy Gap  
492 at  $k = 0$  for a Simple Cubic Ferromagnet with Anisotropic Exchange Interactions.  
493 physica status solidi (b) **102**(1), 365–372 (1980) [https://doi.org/10.1002/pssb.](https://doi.org/10.1002/pssb.2221020135)  
494 [2221020135](https://doi.org/10.1002/pssb.2221020135) <https://onlinelibrary.wiley.com/doi/pdf/10.1002/pssb.2221020135>
- 495 [11] Shender, E.: Anti-ferromagnetic garnets with fluctuation-like interacting sub-  
496 lattices. Zh. Éksp. Teor. Fiz. **83**(1), 326–337 (1982). [Sov. Phys. JETP **56**, 178  
497 (1982)]
- 498 [12] Henley, C.L.: Ordering due to disorder in a frustrated vector antiferromagnet.  
499 Phys. Rev. Lett. **62**, 2056–2059 (1989) [https://doi.org/10.1103/PhysRevLett.62.](https://doi.org/10.1103/PhysRevLett.62.2056)  
500 [2056](https://doi.org/10.1103/PhysRevLett.62.2056)
- 501 [13] Chandra, P., Coleman, P., Larkin, A.I.: Ising transition in frustrated heisenberg  
502 models. Phys. Rev. Lett. **64**, 88–91 (1990) [https://doi.org/10.1103/PhysRevLett.](https://doi.org/10.1103/PhysRevLett.64.88)  
503 [64.88](https://doi.org/10.1103/PhysRevLett.64.88)
- 504 [14] Gvozdkova, M.V., Zhitomirsky, M.E.: A Monte Carlo study of the first-order  
505 transition in a Heisenberg FCC antiferromagnet. Journal of Experimental and  
506 Theoretical Physics Letters **81**(5), 236–240 (2005) [https://doi.org/10.1134/1.](https://doi.org/10.1134/1.1921323)  
507 [1921323](https://doi.org/10.1134/1.1921323)
- 508 [15] Rau, J.G., Lee, E.K.-H., Kee, H.-Y.: Generic Spin Model for the Honeycomb  
509 Iridates beyond the Kitaev Limit. Phys. Rev. Lett. **112**, 077204 (2014) <https://doi.org/10.1103/PhysRevLett.112.077204>  
510 <https://doi.org/10.1103/PhysRevLett.112.077204>
- 511 [16] Shamoto, S.-i., Kodama, K., Harashina, H., Sato, M., Kakurai, K.: Neu-  
512 tron Scattering Study of  $BaCo_{0.82}Ni_{0.18}S_2$ . Journal of the Physical Soci-  
513 ety of Japan **66**(4), 1138–1144 (1997) <https://doi.org/10.1143/JPSJ.66.1138>

- 514 <https://journals.jps.jp/doi/pdf/10.1143/JPSJ.66.1138>
- 515 [17] Shamoto, S.-i., Yamauchi, H., Ikeuchi, K., Kajimoto, R., Ieda, J.: Broken  $C_4$   
516 symmetry in the tetragonal state of uniaxial strained  $\text{BaCo}_{0.9}\text{Ni}_{0.1}\text{S}_{1.9}$ . *Phys. Rev.*  
517 *Research* **3**, 013169 (2021) <https://doi.org/10.1103/PhysRevResearch.3.013169>
- 518 [18] Abushammala, H., Lenz, B., Baptiste, B., Santos-Cottin, D., Toulemonde,  
519 P., Casula, M., Klein, Y., Gauzzi, A.: Two-dimensional fluctuations and  
520 competing phases in the stripe-like antiferromagnet  $\text{BaCoS}_2$ . *arXiv e-prints*,  
521 2302–12208 (2023) <https://doi.org/10.48550/arXiv.2302.12208> [arXiv:2302.12208](https://arxiv.org/abs/2302.12208)  
522 [cond-mat.str-el]
- 523 [19] Mandrus, D., Sarrao, J.L., Chakoumakos, B.C., Fernandez-Baca, J.A., Nagler,  
524 S.E., Sales, B.C.: Magnetism in  $\text{BaCoS}_2$ . *Journal of Applied Physics* **81**(8), 4620–  
525 4622 (1997) <https://doi.org/10.1063/1.365182> <https://doi.org/10.1063/1.365182>
- 526 [20] Syljuåsen, O.F., Paaske, J., Schechter, M.: Interplay between magnetic and vestigi-  
527 al nematic orders in the layered  $J_1 - J_2$  classical Heisenberg model. *Phys. Rev.*  
528 *B* **99**, 174404 (2019) <https://doi.org/10.1103/PhysRevB.99.174404>
- 529 [21] Juhász Junger, I., Ihle, D., Richter, J.: Thermodynamics of layered Heisenberg  
530 magnets with arbitrary spin. *Phys. Rev. B* **80**, 064425 (2009) [https://doi.org/10.](https://doi.org/10.1103/PhysRevB.80.064425)  
531 [1103/PhysRevB.80.064425](https://doi.org/10.1103/PhysRevB.80.064425)
- 532 [22] Santos-Cottin, D., Casula, M., Lantz, G., Klein, Y., Petaccia, L., Le Fèvre, P.,  
533 Bertran, F., Papalazarou, E., Marsi, M., Gauzzi, A.: Rashba coupling amplifi-  
534 cation by a staggered crystal field. *Nature Communications* **7**(1), 11258 (2016)  
535 <https://doi.org/10.1038/ncomms11258>
- 536 [23] Brosco, V., Capone, M.: Rashba-metal to Mott-insulator transition. *Phys. Rev.*  
537 *B* **101**, 235149 (2020) <https://doi.org/10.1103/PhysRevB.101.235149>
- 538 [24] Santos-Cottin, D., Klein, Y., Werner, P., Miyake, T., Medici, L., Gauzzi, A., Lobo,  
539 R.P.S.M., Casula, M.: Linear behavior of the optical conductivity and incoherent  
540 charge transport in  $\text{BaCoS}_2$ . *Phys. Rev. Materials* **2**, 105001 (2018) [https://doi.](https://doi.org/10.1103/PhysRevMaterials.2.105001)  
541 [org/10.1103/PhysRevMaterials.2.105001](https://doi.org/10.1103/PhysRevMaterials.2.105001)
- 542 [25] Snyder, G.J., Gelabert, M.C., DiSalvo, F.J.: Refined Structure and Properties of  
543 the Layered Mott Insulator  $\text{BaCoS}_2$ . *Journal of Solid State Chemistry* **113**(2),  
544 355–361 (1994) <https://doi.org/10.1006/jssc.1994.1380>
- 545 [26] Kodama, K., Shamoto, S.-i., Harashina, H., Takeda, J., Sato, M., Kakurai, K.,  
546 Nishi, M.: Electronic Structure of the Quasi Two-Dimensional Mott System  
547  $\text{BaCo}_{1-x}\text{Ni}_x\text{S}_2$ . *Journal of the Physical Society of Japan* **65**(6), 1782–1786 (1996)  
548 <https://doi.org/10.1143/JPSJ.65.1782> <https://doi.org/10.1143/JPSJ.65.1782>
- 549 [27] Schueller, E.C., Miller, K.D., Zhang, W., Zuo, J.L., Rondinelli, J.M., Wilson,



- 550 S.D., Seshadri, R.: Structural signatures of the insulator-to-metal transition in  
551  $\text{BaCo}_{1-x}\text{Ni}_x\text{S}_2$ . *Phys. Rev. Materials* **4**, 104401 (2020) [https://doi.org/10.1103/](https://doi.org/10.1103/PhysRevMaterials.4.104401)  
552 [PhysRevMaterials.4.104401](https://doi.org/10.1103/PhysRevMaterials.4.104401)
- 553 [28] Zainullina, V.M., Korotin, M.A.: Ground state of  $\text{BaCoS}_2$  as a set of energy-  
554 degenerate orbital-ordered configurations of  $\text{Co}^{2+}$  ions. *Physics of the Solid State*  
555 **53**(5), 978–984 (2011)
- 556 [29] Moreo, A., Dagotto, E., Jolicoeur, T., Riera, J.: Incommensurate correlations in  
557 the t-J and frustrated spin-1/2 Heisenberg models. *Phys. Rev. B* **42**, 6283–6293  
558 (1990) <https://doi.org/10.1103/PhysRevB.42.6283>
- 559 [30] Capriotti, L., Fubini, A., Roscilde, T., Tognetti, V.: Ising Transition in the Two-  
560 Dimensional Quantum  $J_1 - J_2$  Heisenberg Model. *Phys. Rev. Lett.* **92**, 157202  
561 (2004) <https://doi.org/10.1103/PhysRevLett.92.157202>
- 562 [31] Weber, C., Becca, F., Mila, F.: Finite-temperature properties of frustrated classi-  
563 cal spins coupled to the lattice. *Phys. Rev. B* **72**, 024449 (2005) [https://doi.org/](https://doi.org/10.1103/PhysRevB.72.024449)  
564 [10.1103/PhysRevB.72.024449](https://doi.org/10.1103/PhysRevB.72.024449)
- 565 [32] Lante, V., Parola, A.: Ising phase in the  $J_1 - J_2$  Heisenberg model. *Phys. Rev. B*  
566 **73**, 094427 (2006) <https://doi.org/10.1103/PhysRevB.73.094427>
- 567 [33] Oitmaa, J., Enting, I.G.: Critical behaviour of the anisotropic Ising model. *Jour-  
568 nal of Physics C: Solid State Physics* **5**(2), 231 (1972) [https://doi.org/10.1088/](https://doi.org/10.1088/0022-3719/5/2/012)  
569 [0022-3719/5/2/012](https://doi.org/10.1088/0022-3719/5/2/012)
- 570 [34] Fernandes, R.M., Chubukov, A.V., Schmalian, J.: What drives nematic order in  
571 iron-based superconductors? *Nature Physics* **10**(2), 97–104 (2014) [https://doi.](https://doi.org/10.1038/nphys2877)  
572 [org/10.1038/nphys2877](https://doi.org/10.1038/nphys2877)
- 573 [35] Wang, F., Kivelson, S.A., Lee, D.-H.: Nematicity and quantum paramagnetism in  
574  $\text{FeSe}$ . *Nature Physics* **11**(11), 959–963 (2015) <https://doi.org/10.1038/nphys3456>
- 575 [36] Kothapalli, K., Böhmer, A.E., Jayasekara, W.T., Ueland, B.G., Das, P., Sapkota,  
576 A., Taufour, V., Xiao, Y., Alp, E., Bud’ko, S.L., Canfield, P.C., Kreyssig, A.,  
577 Goldman, A.I.: Strong cooperative coupling of pressure-induced magnetic order  
578 and nematicity in  $\text{FeSe}$ . *Nature Communications* **7**(1), 12728 (2016) [https://doi.](https://doi.org/10.1038/ncomms12728)  
579 [org/10.1038/ncomms12728](https://doi.org/10.1038/ncomms12728)
- 580 [37] Chubukov, A.V., Efremov, D.V., Eremin, I.: Magnetism, superconductivity, and  
581 pairing symmetry in iron-based superconductors. *Phys. Rev. B* **78**, 134512 (2008)  
582 <https://doi.org/10.1103/PhysRevB.78.134512>
- 583 [38] Stanev, V., Kang, J., Tesanovic, Z.: Spin fluctuation dynamics and multiband  
584 superconductivity in iron pnictides. *Phys. Rev. B* **78**, 184509 (2008) [https://doi.](https://doi.org/10.1103/PhysRevB.78.184509)  
585 [org/10.1103/PhysRevB.78.184509](https://doi.org/10.1103/PhysRevB.78.184509)

- 586 [39] Graser, S., Maier, T.A., Hirschfeld, P.J., Scalapino, D.J.: Near-degeneracy of sev-  
587 eral pairing channels in multiorbital models for the Fe pnictides. *New Journal of*  
588 *Physics* **11**(2), 025016 (2009) <https://doi.org/10.1088/1367-2630/11/2/025016>
- 589 [40] Hu, J., Xu, B., Liu, W., Hao, N.-N., Wang, Y.: Unified minimum effective model  
590 of magnetic properties of iron-based superconductors. *Phys. Rev. B* **85**, 144403  
591 (2012) <https://doi.org/10.1103/PhysRevB.85.144403>
- 592 [41] Glasbrenner, J.K., Mazin, I.I., Jeschke, H.O., Hirschfeld, P.J., Fernandes, R.M.,  
593 Valentí, R.: Effect of magnetic frustration on nematicity and superconductivity  
594 in iron chalcogenides. *Nature Physics* **11**(11), 953–958 (2015) [https://doi.org/10.](https://doi.org/10.1038/nphys3434)  
595 [1038/nphys3434](https://doi.org/10.1038/nphys3434)
- 596 [42] Zhao, J., Adroja, D.T., Yao, D.-X., Bewley, R., Li, S., Wang, X.F., Wu, G., Chen,  
597 X.H., Hu, J., Dai, P.: Spin waves and magnetic exchange interactions in  $\text{CaFe}_2\text{As}_2$ .  
598 *Nature Physics* **5**(8), 555–560 (2009) <https://doi.org/10.1038/nphys1336>
- 599 [43] Giannozzi, P., Baroni, S., Bonini, N., Calandra, M., Car, R., Cavazzoni, C.,  
600 Ceresoli, D., Chiarotti, G.L., Cococcioni, M., Dabo, I., Corso, A.D., Giron-  
601 coli, S., Fabris, S., Fratesi, G., Gebauer, R., Gerstmann, U., Gougoussis, C.,  
602 Kokalj, A., Lazzeri, M., Martin-Samos, L., Marzari, N., Mauri, F., Mazzarello, R.,  
603 Paolini, S., Pasquarello, A., Paulatto, L., Sbraccia, C., Scandolo, S., Sclauzero,  
604 G., Seitsonen, A.P., Smogunov, A., Umari, P., Wentzcovitch, R.M.: QUANTUM  
605 ESPRESSO: a modular and open-source software project for quantum simula-  
606 tions of materials. *Journal of Physics: Condensed Matter* **21**(39), 395502 (2009)  
607 <https://doi.org/10.1088/0953-8984/21/39/395502>
- 608 [44] Giannozzi, P., Andreussi, O., Brumme, T., Bunau, O., Nardelli, M.B., Calandra,  
609 M., Car, R., Cavazzoni, C., Ceresoli, D., Cococcioni, M., Colonna, N., Carnimeo,  
610 I., Corso, A.D., Gironcoli, S., Delugas, P., DiStasio, R.A., Ferretti, A., Floris,  
611 A., Fratesi, G., Fugallo, G., Gebauer, R., Gerstmann, U., Giustino, F., Gorni,  
612 T., Jia, J., Kawamura, M., Ko, H.-Y., Kokalj, A., Küçükbenli, E., Lazzeri, M.,  
613 Marsili, M., Marzari, N., Mauri, F., Nguyen, N.L., Nguyen, H.-V., Otero-de-la-  
614 Roza, A., Paulatto, L., Poncé, S., Rocca, D., Sabatini, R., Santra, B., Schlipf, M.,  
615 Seitsonen, A.P., Smogunov, A., Timrov, I., Thonhauser, T., Umari, P., Vast, N.,  
616 Wu, X., Baroni, S.: Advanced capabilities for materials modelling with Quantum  
617 ESPRESSO. *Journal of Physics: Condensed Matter* **29**(46), 465901 (2017) <https://doi.org/10.1088/1361-648x/aa8f79>  
618
- 619 [45] Perdew, J.P., Burke, K., Ernzerhof, M.: Generalized Gradient Approximation  
620 Made Simple. *Phys. Rev. Lett.* **77**, 3865–3868 (1996) [https://doi.org/10.1103/](https://doi.org/10.1103/PhysRevLett.77.3865)  
621 [PhysRevLett.77.3865](https://doi.org/10.1103/PhysRevLett.77.3865)
- 622 [46] Anisimov, V.I., Zaanen, J., Andersen, O.K.: Band theory and Mott insulators:  
623 Hubbard U instead of Stoner I. *Phys. Rev. B* **44**, 943–954 (1991) [https://doi.org/](https://doi.org/10.1103/PhysRevB.44.943)  
624 [10.1103/PhysRevB.44.943](https://doi.org/10.1103/PhysRevB.44.943)

- 625 [47] Liechtenstein, A.I., Anisimov, V.I., Zaanen, J.: Density-functional theory and  
626 strong interactions: Orbital ordering in Mott-Hubbard insulators. *Phys. Rev. B*  
627 **52**, 5467–5470 (1995) <https://doi.org/10.1103/PhysRevB.52.R5467>
- 628 [48] Marzari, N., Vanderbilt, D.: Maximally localized generalized Wannier functions  
629 for composite energy bands. *Phys. Rev. B* **56**, 12847–12865 (1997) <https://doi.org/10.1103/PhysRevB.56.12847>  
630
- 631 [49] Souza, I., Marzari, N., Vanderbilt, D.: Maximally localized Wannier functions  
632 for entangled energy bands. *Phys. Rev. B* **65**, 035109 (2001) <https://doi.org/10.1103/PhysRevB.65.035109>  
633
- 634 [50] Mostofi, A.A., Yates, J.R., Pizzi, G., Lee, Y.-S., Souza, I., Vanderbilt, D., Marzari,  
635 N.: An updated version of wannier90: A tool for obtaining maximally-localised  
636 Wannier functions. *Computer Physics Communications* **185**(8), 2309–2310 (2014)  
637 <https://doi.org/10.1016/j.cpc.2014.05.003>
- 638 [51] Kanada, M., Harashina, H., Sasaki, H., Kodama, K., Sato, M., Kakurai, K., Nishi,  
639 M., Nishibori, E., Sakata, M., Takata, M., Adachi, T.: High-pressure neutron and  
640 X-ray studies on the Mott transition of BaCoS<sub>2</sub>. *Journal of Physics and Chem-*  
641 *istry of Solids* **60**(8), 1181–1183 (1999) [https://doi.org/10.1016/S0022-3697\(99\)](https://doi.org/10.1016/S0022-3697(99)00078-5)  
642 [00078-5](https://doi.org/10.1016/S0022-3697(99)00078-5)

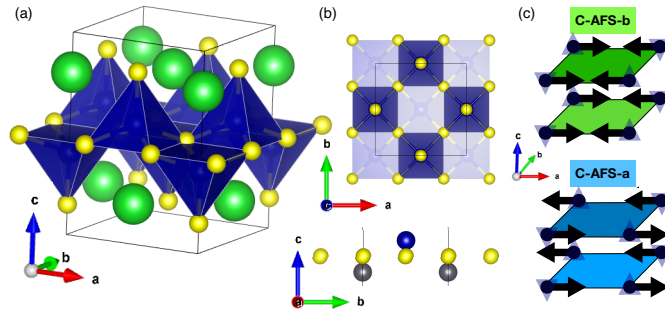


**Fig. 1 Crystal structure of  $\text{BaCoS}_2$ .** (a) Three-dimensional view of tetragonal  $\text{BaCoS}_2$ . Ba atoms are the large green spheres, while S atoms are shown in yellow. The cobalt atoms sit inside the blue square-based pyramids. (b) Top and lateral view of the structure, respectively. Note that, since the apexes of nearest neighbour pyramids point in opposite directions, there are two inequivalent Co atoms, shown as blue and grey spheres, with opposite vertical displacements from the  $a - b$  plane, which are connected by the non-symmorphic symmetry. (c) Magnetic order in the low-temperature orthorhombic phase. Dots represent Co atoms, arrows their spins and blue triangles indicate the orientation of the surrounding sulfur pyramids. Within each  $a - b$  plane the spins form a striped antiferromagnet (AFS) with ferromagnetic chains coupled antiferromagnetically. The ferromagnetic chains can be either along  $a$  (AFS-a) or along  $b$  (AFS-b). The planes are stacked ferromagnetically, C-type stacking, thus the two equivalent configurations C-AFS-a and C-AFS-b.

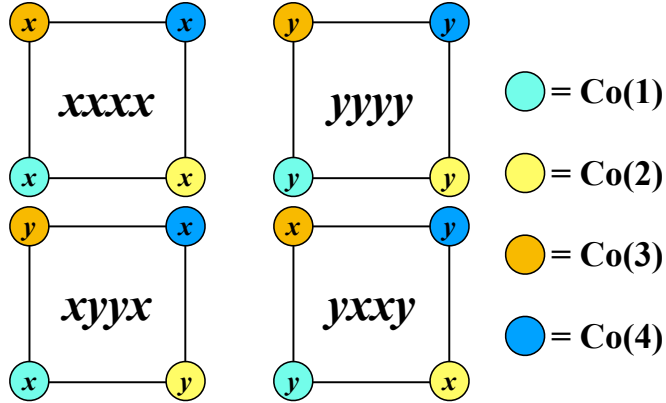


**Fig. 2** Illustration of the orbital arrangements within  $\text{BaCoS}_2$  allowed by the  $Cmme$  space group. Co(1), Co(2), Co(3) and Co(4) correspond to the  $4g$  Wyckoff positions occupied by the cobalt atoms. The label  $x(y)$  indicates that the hole occupies the  $d_{xz}(d_{yz})$  orbital of the  $3/4$ -filled  $d_{xz}/d_{yz}$  doublet of the corresponding cobalt atom.

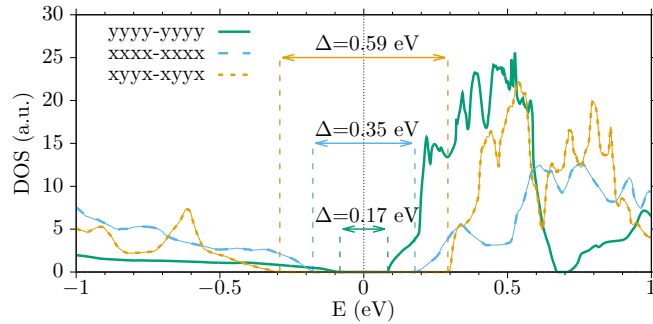


**Fig. 3** Density of states for different orbital configurations. The density of states (DOS) around the Fermi level is shown for the two orbital nematic configurations  $yyyy$  (full green line) and  $xxxx$  (dashed blue line) as well as for the orbital ordered configuration  $xyyx$  (dashed orange line), which is found to be lowest in energy within Hubbard- $U$  corrected density functional theory (DFT+ $U$ ) calculations.

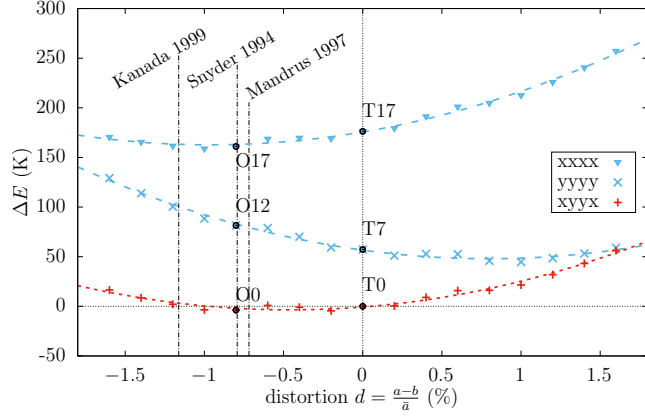


**Fig. 4 Phase stability upon orthorhombic distortions.** Energy  $\Delta E$  per formula unit as function of the orthorhombic distortion  $d$  at fixed unit cell volume and measured with respect to the  $C(xyxx)$  phase at  $d = 0$  (T0 in Table 1). We compare  $C(xyxx)$  with the two nematic configurations  $C(xxxx)$  and  $C(yyyy)$  assuming a magnetic order C-AFS-a. Experimental data are taken from Refs. [19, 25, 51]. The phases T0, T7, and T17 refer to Table 1, phases O0, O12, and O17 to Table 3.

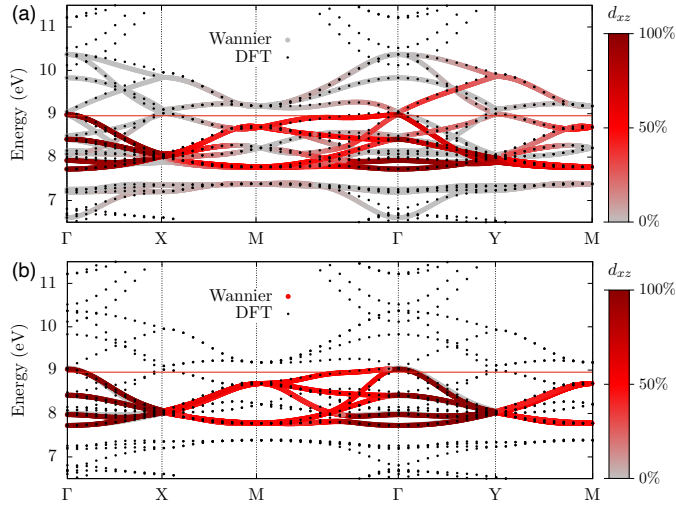


**Fig. 5 Wannierization of the density functional theory (DFT) band structure.** DFT band structure and eigenstates of our Wannier Hamiltonians along the high-symmetry path  $\Gamma - X - M - \Gamma - Y - M$ : (a) Co- $d$  model and (b)  $d_{xz}$ - $d_{yz}$  model with projection onto the  $d_{xz}$ -orbital character in red.

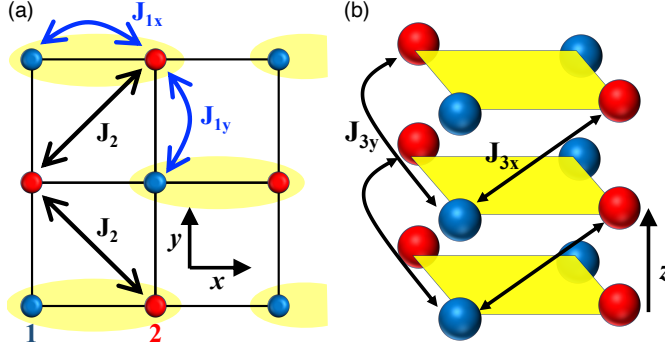


**Fig. 6** Effective Heisenberg spin model for  $\text{BaCoS}_2$ . Panel (a) shows the  $J_1 - J_2$  model on the  $a - b$  plane, while panel (b) shows how nearest neighbour planes are coupled to each other by the exchange  $J_3$ . The latter forces to deal with a two-site unit cell, highlighted in yellow in panel (a). Blue and red balls indicate the two different Co sites of the unit cell.

spin and orbital configurations	$E(\text{Kelvin})$	#
C-AFS-a-C( $xyyx$ )	0	T0
G-AFS-a-C( $xyyx$ )	2	T1
C-AFS-a-G( $xyyx$ )	14	T2
G-AFS-a-G( $xyyx$ )	22	T3
G-AFS-a-G( $xyxy$ )	50	T4
C-AFS-a-G( $xyxy$ )	52	T5
C-AFS-a-C( $xyxy$ )	52	T6
C-AFS-a-C( $yyyy$ )	57	T7
G-AFS-a-C( $xyxy$ )	64	T8
G-AFS-a-C( $yyyy$ )	73	T9
C-AFS-a-G( $xyyy$ )	79	T10
C-AFS-a-G( $yyyy$ )	86	T11
G-AFS-a-G( $yyyy$ )	89	T12
G-AFS-a-C( $xyyy$ )	89	T13
C-AFS-a-C( $xyyy$ )	93	T14
G-AFS-a-G( $xyyy$ )	95	T15
G-AFS-a-C( $xxxx$ )	171	T16
C-AFS-a-C( $xxxx$ )	176	T17

**Table 1** *Ab initio* energies of the tetragonal phase. Hubbard- $U$  corrected density functional theory (DFT+ $U$ ) energies ( $U = 2.8$  eV) in Kelvin and per formula unit of the low-lying spin and orbital configurations in the tetragonal structure with an 8-site unit cell, assuming an antiferromagnetic stripe order along  $a$  (AFS- $a$ ), being degenerate with AFS- $b$ . The lowest energy state sets the zero of energy. Note that some states are doubly degenerate, for instance  $C(xyyx)$  is degenerate with  $C(yxyx)$  as well as  $G(yyyy)$  is degenerate with  $G(xxxx)$ , and thus we just indicate one of them. Moreover, the table includes also configurations not allowed by the  $Cmme$  orthorhombic space group, which, nonetheless, represent alternative symmetry-breaking paths from the tetragonal structure. Each state is labelled by  $Tn$ , T referring to the tetragonal phase and  $n$  being the ascending order in energy.

(a)

orbital configuration	$E$	$\Delta E$
$yyx$	$-2\Gamma_1$	0
$xyxy$	$-2\sigma\delta\Gamma_1$	$2\Gamma_1 - 2\sigma\delta\Gamma_1$
$xyxy$	$2\sigma\delta\Gamma_1$	$2\Gamma_1 + 2\sigma\delta\Gamma_1$
$xxx$	$2\Gamma_1 - \sigma B_\tau$	$4\Gamma_1 - \sigma B_\tau$
$yyy$	$2\Gamma_1 + \sigma B_\tau$	$4\Gamma_1 + \sigma B_\tau$

(b)

	$\Gamma_1$ (K)	$\delta\Gamma_1$ (K)	$B_\tau$ (K)
C-AFS	$33 \pm 4$	10	60
G-AFS	$31 \pm 4$	6	49

**Table 2 Ising model for the**

**tetragonal phase.** The energies of the different orbital configurations within an assumed nearest neighbour antiferromagnetic Ising model with exchange constants  $\Gamma_1 + \sigma\delta\Gamma_1$  along  $a$ ,  $\Gamma_1 - \sigma\delta\Gamma_1$  along  $b$ , and uniform pseudo-magnetic field  $\sigma B_\tau$  are listed in (a). The values of those parameters extracted through Table 1 for antiferromagnetic stripe (AFS) ordering are shown in (b). We just consider the C-type orbital stacked configurations, since the G-type ones do not allow fixing  $B_\tau$ .



spin and orbital configurations	$E(\text{Kelvin})$	#
C-AFS-a-C( $xyyx$ )	0	O0
G-AFS-a-C( $xyyx$ )	2	O1
C-AFS-a-G( $xyyx$ )	14	O2
C-AFS-b-C( $xyyx$ )	20	O3
G-AFS-a-G( $xyyx$ )	22	O4
G-AFS-b-C( $xyyx$ )	22	O5
C-AFS-b-G( $xyyx$ )	34	O6
G-AFS-b-G( $xyyx$ )	42	O7
C-AFS-b-C( $xxxx$ )	50	O8
G-AFS-b-C( $xxxx$ )	65	O9
C-AFS-b-G( $xxxx$ )	79	O10
G-AFS-b-G( $xxxx$ )	82	O11
C-AFS-a-C( $yyyy$ )	85	O12
C-AFS-a-G( $xxxx$ )	93	O13
G-AFS-a-G( $xxxx$ )	96	O14
G-AFS-a-C( $yyyy$ )	101	O15
G-AFS-a-C( $xxxx$ )	160	O16
C-AFS-a-C( $xxxx$ )	165	O17
G-AFS-b-C( $yyyy$ )	203	O18
C-AFS-b-C( $yyyy$ )	209	O19

**Table 3 Ab initio energies of the orthorhombic phase.** Same as in Table 1 but for the orthorhombic structure with  $b > a$ ,  $b/a = 1.008$ . In this case, antiferromagnetic stripe order along  $a$  (AFS-a) and AFS-b are not degenerate, and thus both have been studied. Only the orbital configurations allowed by symmetry are shown. The states are labelled by  $On$ , where O refers to the orthorhombic phase and  $n$  is the order.

bond direction	hopping matrix (meV)
$T_{(1,1,0)} = T_{(-1,-1,0)}$	$\begin{pmatrix} 96 & 102 \\ 102 & 94 \end{pmatrix}$
$T_{(1,-1,0)} = T_{(-1,1,0)}$	$\begin{pmatrix} 96 & -102 \\ -102 & 94 \end{pmatrix}$
$T_{(1,0,0)} = T_{(-1,0,0)}$	$\begin{pmatrix} 2 & 0 \\ 0 & -43 \end{pmatrix}$
$T_{(0,1,0)} = T_{(0,-1,0)}$	$\begin{pmatrix} -48 & 0 \\ 0 & 2 \end{pmatrix}$
$T_{(1,0,1)} = T_{(-1,0,1)}$	$\begin{pmatrix} -68 & 0 \\ 0 & 18 \end{pmatrix}$
$T_{(0,1,1)} = T_{(0,-1,1)}$	$\begin{pmatrix} 20 & 0 \\ 0 & -69 \end{pmatrix}$

**Table 4 Hopping amplitudes within the two-orbital submanifold.** Leading hopping processes  $T_{(n_x, n_y, n_z)}$ , where  $\mathbf{r} = (n_x, n_y, n_z)$  identifies the bond connecting Co(1), see Fig. 2, to another cobalt at distance  $\mathbf{r}$ . The bonds emanating from Co(2) are obtained by the non-symmorphic symmetry, which, in particular, implies  $n_z \rightarrow -n_z$ . All hopping processes are written as matrices in the subspace  $(d_{xz}, d_{yz})$ . The values, in meV, are obtained by the 5-orbital model restricted to the  $(d_{xz}, d_{yz})$  subspace.